POLITECNICO MILANO 1863 | SCHOOL OF INDUSTRIAL AND INFORMATION ENGINEERING

Computational Fluid Dynamics – A.A. 2024-2025

CFD Investigation of Gurney Flap Effects on an Airfoil

Aloisi Lorenzo Angelo, 10707761
Guerrieri Tommaso, 10731212
Piomboni Luca, 11011639
Tommasi Alessandro, 10700642

Group number N 20

Lecturers:
Dr. Barbara Re
Dr. Andrea Rausa

1. Problem statement

The aim of our project is to evaluate the effect of a Gurney flap on a NACA 0021 downforce profile, investigating the aerodynamic coefficients at a fixed Reynolds number of 180'000, with a focus on their comparison when using different turbulence models.
The CFD model is validated with wind tunnel data of the same profile but in lifting operational case (with the Gurney flap placed on the lower surface) as proposed by J.Balduzzi et Al.[1]. This comparison was possible simply reverting the sign of the lift coefficients since the flap is fitted on a symmetrical airfoil.

1.1. Physics of the problem

The Gurney flap was conceived over three decades ago by race car campaigner Dan Gurney as a lift enhancement device used to increase the downforce provided by the wing of his Indianapolis 500 car. It is a passive flow-control device traditionally mounted on the pressure side of the trailing edge and with an height generally ranging between 1% and 5% of the airfoil chord. It has been widely studied since Liebeck's [4] research revealed its beneficial effects.
He found out that the Gurney forces the flow to turn towards the flap and so that produce two counter rotating vortices which increase the lift (or downforce as in our case), despite adding a drag penalty. When the flow approaches a lifting profile, on the lower surface the flow separates before the Gurney, creating a bubble and forming a recirculation zone which extends to the apex of the Gurney flap.
Simultaneously, flow separating from the upper surface trailing-edge, together with the flow separating downstream of the Gurney apex, forms a downstream recirculation region composed of two counter-rotating vortices. This recirculation region produces a stagnation point downstream of the trailing-edge that is deflected downward (Figure 1).
Although the qualitative effect of the Gurney is well-known, the theoretical basis was put forward to explain its effect on airfoil lift. According to thin airfoil theory by Liu et Al.[6] Gurney flap lift enhancement is interpreted as a special camber effect.
At low Re, stable vortex structures comparable to those hypothesized by Liebeck can be found downstream of bluff bodies. However, when higher values are matched, vortex shedding arise. Actually, when the unstable shedding structure is averaged over time, the alternating velocities downstream of the body cancel out, and the only evidence of the vortex shedding is found close to the base. Here, the time-averaged flow pattern consists of two counter-rotating vortices and is similar to that vortical features predicted by Liebeck for the Gurney.

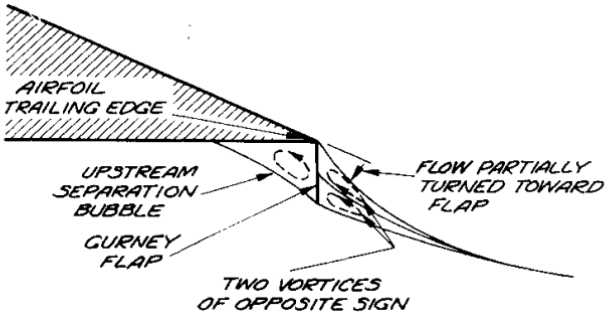

Figure 1: Hypothesized trailing-edge flow conditions of the Gurney according to Liebeck [4].

1.2. Hypothesis

The selected case study for our analysis is a NACA 0021 airfoil with a unitary chord length (c). The configuration of the Gurney flap is the one of a downforce profile for automotive application, therefore the positive angles in the project are taken in the counter-clockwise direction (opposite sign convention to that typically used in the literature). The flap is a one-sided perpendicular tab, with an height of 1.4%c according to the referenced paper of J.Balduzzi et Al.[1]. All the simulations were performed with a steady-state condition at Re = 180'000, using RANS incompressible turbulence models such as $k-\omega$ SST and Spalart-Allmaras (both at different order of accuracy), and for each of these the strength and weaknesses are underlined in Section 3.3.

2. Simulation methodology

In this section, we outline the pre-processing steps and the setup of the simulation.

- In Subsection 2.1, the focus is on mesh generation using *Gmsh*.
- Subsection 2.2 describes the solver algorithms and numerical methods, including all settings specified in the `config` file, boundary conditions included.

Of particular interest is the approach discussed in Subsection 2.2.1, which investigates how SU2, primarily designed for compressible and high-Mach flows, adapts to incompressible simulations. The decision to focus on this specific incompressible case was motivated by the desire to expand our understanding of SU2's applicability to incompressible flow scenarios.
Finally, Subsection 2.2.2 details the numerical schemes used to compute the fluxes, providing a clear and concise explanation. These schemes are necessary due to the adoption of a finite volume method (FVM). As already said, turbulence was taken into account trough the use of RANS equations.

2.1. Mesh Generation

The numerical mesh is realized using the open source software *Gmsh*. The domain is discretized through a multi-block O-grid, with a radius of 50 chord length, and a hybrid grid shape composed by triangular finite volumes elements everywhere apart from the boundary layer's cells that are rectangular. This choice produces a better simulation of the flow close to the wall.
Since the flow close to the airfoil is solved without resorting to wall functions, a $y^+ < 1$ condition is enforced all over the geometry. The boundary layer is realized inflating a total of 20 layers, the first with a thickness of $6.66 \cdot 10^{-5}\, m$ and an expansion ratio of 1.19. Due to limitations of the meshing software to match the boundary layer on the upper and front sides of the Gurney flap, triangular cells are used in these regions (Figure 2c).
This choice is justified by the presence of a separated region immediately before and past the flap, as will be shown in the τ_{wall} visualization (Figure 9) there are null values in some of the nearby areas. To obtain such arrangement a trapezoidal block is created in order to have a better conjunction with the structured boundary layer and an additional block is also added in the trailing edge area to joint

the wake region with the lower part of the airfoil.
To better capture the behavior of the wake, two levels of refinements are adopted as in Figure 2b. The first extending one chord length ahead the leading edge and 50 past the trailing edge, while a finer one extends 0.3 chord length forward and 2 chord past the body. The remaining part of the fluid domain gets coarser and coarser as we reach the far field where the flow is uniform (Figure 2a).

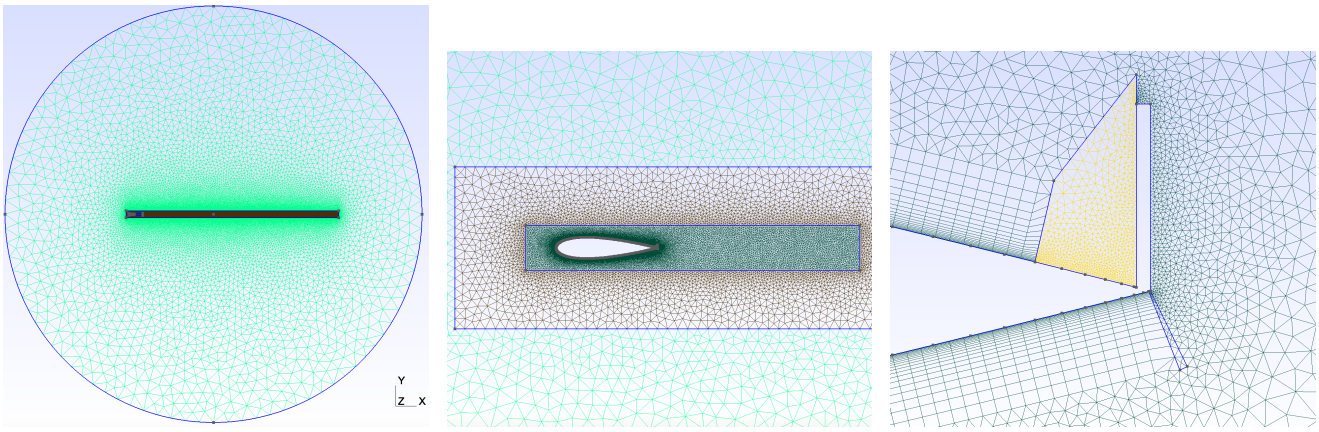

(a) O-grid. (b) Refinement boxes. (c) Detail of the trailing edge.

Figure 2: Show in detail the baseline mesh used for the simulations.

This mesh is later used by SU2 to create a secondary grid, polygonal and node-centered, used to perform the actual computations.
To be precise, validation and turbulence models comparisons (Sections 3.2, 3.3) are carried out using a baseline grid made of about 120'000 cells, while two finer meshes are required to guarantee and demonstrate grid convergence. Unfortunately, due to limited computational resources, it was not possible to conduct all simulations with the extra-fine one.

2.2. Numerical Methods and Algorithms

This section outlines the methodology and configuration employed for the simulation. Key aspects of the setup, including boundary conditions, are briefly described to provide an overview of the computational framework.
Concerning the boundary conditions, a no slip condition is used for the airfoil; the chosen flow velocity modulus is 2.61 m/s (in the whole far-field), which combined with unitary chord and air properties in standard conditions gives back a Reynolds number of 180'000 consistently with experimental conditions. The heat fluxes are null on the walls.
The regime under consideration is incompressible, given the low-speed nature of the flow; but as we'll see, the need to impose a temperature-related boundary condition (in this case the heat-flux on the wall) is linked on how the solver in SU2 deals with incompressible RANS.
In fact,as said, part of the interest behind the choice of this specific study is related to the analysis of the performance and numerical approach of SU2 under conditions characterized by low-speed, incompressible flow. By doing so, we aim to understand how a software majorly designed with compressible flow dynamics in mind (characterized by high Reynolds and high Mach number and *Riemann invariants solvers*) adapts to a regime where compressibility effects are negligible. It's very interesting the approach proposed in SU2 to deal with incompressible flows, both laminar and turbulent.

2.2.1 The Approach: Variable Density Incompressible Flows

Based on SU2 documentation and insights from T. D. Economon [3], we present a concise overview of the solver's procedure. While this approach might be slightly computationally expensive for strictly incompressible flows (like the case we are analyzing), it was selected by the developers for its versatility

and ability to handle low-Mach-number flows, where slight variations in density and temperature play a significant role.
Low-Mach flows pose unique challenges, as outlined below:

- A standard treatment using *Riemann invariants* can lead to significant stiffness in convergence due to the **high condition number** of the system matrix. This stiffness arises because the characteristic timescales (and propagation speeds) of the various waves differ substantially, with the acoustic wave speed being much higher than the fluid velocity at low Mach numbers. For fully incompressible flows, this problem becomes even more pronounced due to the absence of time-dependent density or pressure variations which implies also the non hyperbolicity of the system.
- A traditional pressure-velocity coupling approach, such as Chorin's *pressure projection*, would require a complete redesign of SU2's solvers to accommodate incompressible flows. This would detract from the flexibility and uniformity of the framework, particularly when adapting to other flow regimes.

The approach implemented in SU2 introduces the concept of **artificial compressibility**. By incorporating a temporal derivative of pressure, the equations are transformed into a quasi-hyperbolic form. This transformation not only aligns well with numerical methods typically used for compressible solvers in SU2, but also reduces the condition number of the system matrix, facilitating faster and more robust convergence.

2.2.2 The schemes

This section addresses the numerical convective schemes used for both the flow and turbulence equations. It is important to note that incompressible flow solvers offer a limited selection of schemes, primarily restricted to the Flux Difference Splitting (FDS) and Jameson-Schmidt-Turkel (JST) methods.
Initially, we employed the JST scheme with low-speed preconditioning. However, this approach proved unsuitable for our case. The primary issue lies in the nature of the JST scheme, which is specifically designed for transonic and supersonic regimes and assumes steady-state flows. In our scenario, the presence of a Gurney flap induces significant flow separation upstream of itself, leading to inherently unsteady behavior.
While low-speed preconditioning with adaptive coefficients may adequately address the challenges due to low speed conditions, the assumption of steady-state conditions diverges substantially from the actual flow dynamics around a Gurney flap. Consequently, the JST scheme is fundamentally misaligned with the unsteady nature of the problem under consideration.
Starting from these considerations, we moved to **FDS**. Here we propose the wave propagation form:

$$U_j^{n+1} = U_j^n - \frac{\Delta t}{\Delta x}\left(\mathcal{A}^+ \Delta U_{j-1/2} + \mathcal{A}^- \Delta U_{j+1/2}\right)$$

In flux difference form, we get to:

$$\Delta x \frac{dU_j}{dt} = -\Delta f^-_{j-\frac{1}{2}} + \Delta f^-_{j+\frac{1}{2}}$$

It is necessary to remind that for a case like this, where we are dealing with steady RANS, it cannot be said that there is a real time marching, but rather all time derivatives are related to a **pseudo time-stepping** procedure.
Initially, a **first-order numerical scheme** was used to solve the governing equations for the flow (mass, momentum, and energy), without employing a `MUSCLE` (Monotonic Upstream-Centered Scheme for Conservation Laws) reconstruction.
However, this approach significantly underpredicted the drag values, primarily due to its inability to accurately resolve the steep gradients near the Gurney flap.
The mathematical reasoning behind this underprediction lies in the excessive numerical diffusion inherent in first-order schemes. This diffusion leads to a smearing of the solution near the flap, particularly

reducing the pressure peak observed upstream of the Gurney flap. Consequently, the pressure drag is substantially underestimated.
To address this issue and improve the accuracy of the drag prediction, a **second-order numerical scheme** was implemented to better capture the steep gradients and flow physics around the Gurney flap.
As for the turbulence modeling, both **first-order** and **second-order** approaches are explored, and the details of this investigation are presented in the next section.

3. Results

In this section we report and discuss the main results of our simulations. They are divided into two parts: firstly we present grid convergence and validation of our simulations to prove their correctness and reliability. Finally there will be a deep analysis of the actual results with the goal of answer the questions proposed in Section 1.

3.1. Grid convergence

To demonstrate grid convergence, we have performed five simulations at 0° AOA with the same settings while using different meshes with different refinements. The grids are refined uniformly doubling the sizes at each iteration. The results are presented by means of the charts below in Figures 3 and 4.
In Figure 3a is plotted the lift coefficient versus the non dimensional parameter $1/\sqrt{N_{\text{cells}}}$ characteristic of each grid, while in Figure 3b the convergence of pressure coefficient w.r.t. a curvilinear abscissa (S) along the airfoil perimeter can be observed.
In the first mentioned figure we can observe that the grid convergence is not fully reached even though the data show a good trend, while in the second it is possible to notice how the fine and the extra-fine lines are almost coincident, and this holds even in the Gurney flap region where strong gradients are present.
It is worth to point out a further observation: it is evident from Figure 3a that the changes in the overall variable C_l are significant as the mesh size changes. The local contribution to this behavior can be analyzed with more care looking a the results in Figure 3b, where it is shown that the differences in the local value of C_p between the various meshes. We see that the most visible changes are localized mainly near the flap.
This analysis confirms that the introduction of such a small element generates substantial challenges not only in the meshing process but also in the numerical computation. A lack of precision in this region (as seen with the coarse mesh) can lead to errors of more than 10% in the lift coefficient prediction.

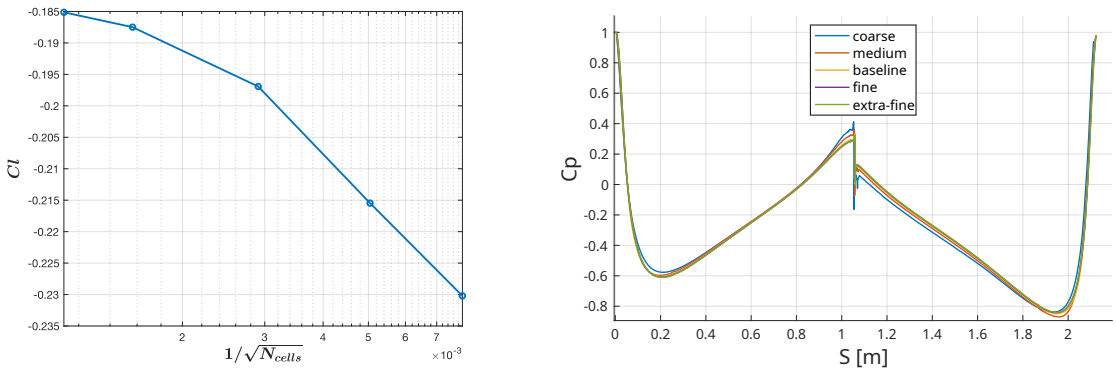

(a) Cl vs. non dimensional parameter.

(b) C_p vs. curvilinear abscissa.

Figure 3: Grid convergence.

Finally, Figure 4 illustrates the behavior of the residuals for each case, providing further insight into the numerical performance and convergence quality for the different meshes.

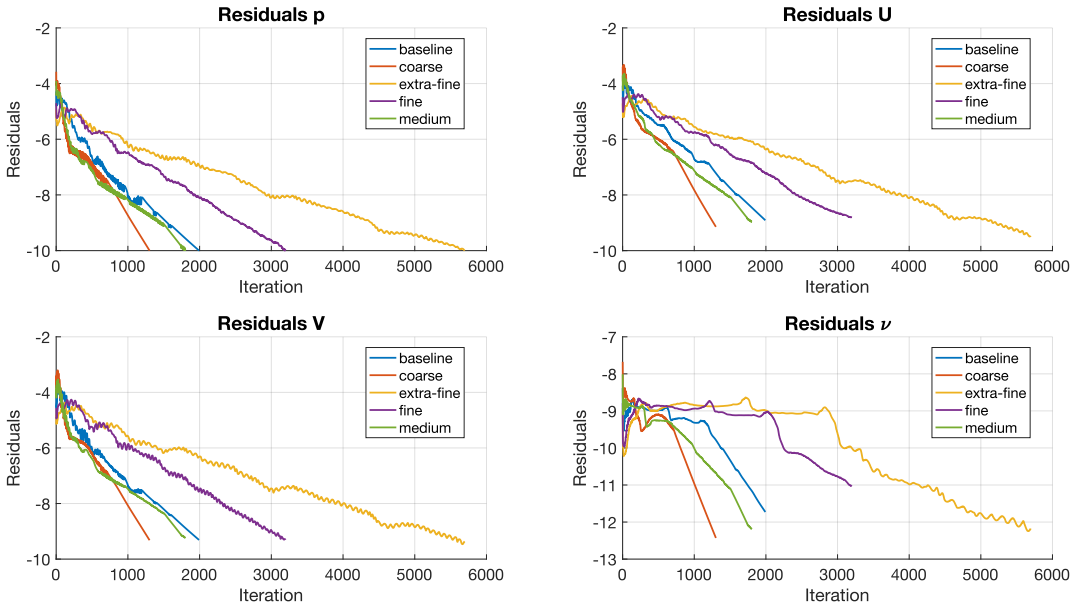

Figure 4: Comparison residuals among different overall grid dimension refinements at $\alpha = 0°$.

The residuals control is performed on the pressure and the simulations are considered converged when a value of 10^{-10} is reached.
Figure 4 shows an oscillatory behavior of the residuals and this is partially related to the implicit unsteadiness of the phenomena,that doesn't ensure a smooth convergence and in part due to the quality of the mesh that is not so precise, particularly in the region where the boundary layer connects with the triangles (Figure 2c). Unfortunately the poor capabilities of *Gmsh* did not allow us to improve further our discretization.

3.2. Validation

For the validation process we compared the results of our simulations against the experimental data obtained by J.Balduzzi et Al [1].
We used the Spalart–Allmaras turbulence model at the 2^{nd} order as baseline for our validations since it is the best one to simulate such kind of problem, as it will be shown in Subsection 3.3. The validation results are reported in Figure 5.

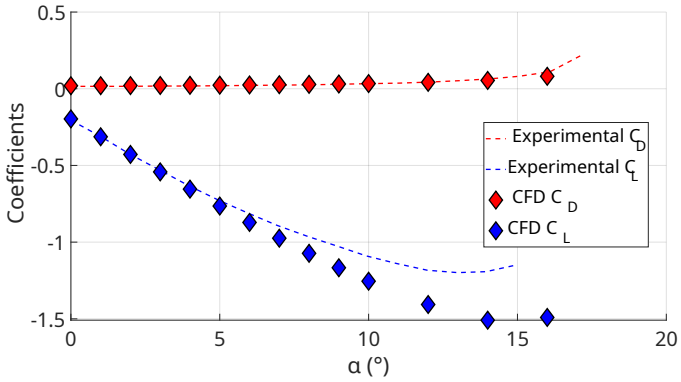

Figure 5: Comparison experimental data on the lift and drag coefficients versus results of our CFD analysis.

We can see from the plot that the results are extremely accurate for what concern the drag, while for the lift we obtain an optimum fit of the data for low values of the angle of attack, up to $\alpha \approx 4°$, then

they start to diverge.
This behavior is absolutely reasonable considering the fact that the turbulence model used here (SA) is able to predict well the correctness of the solution up to small angles of attack, in the limit of small turbulent effects and not big separations. For this reason the simulation cannot access angles that go beyond the stall, and indeed after approximately $\alpha = 16°$ the simulation completely diverges.
When looking to these data we must also account for the fact that the reference geometry we considered in the paper of J.Balduzzi et Al. [1] is slightly different from ours due to both incompleteness of the data provided in the paper itself, and simplifications introduced. For this reasons the results come are already with an error.

After all these considerations we can assume with sufficient certainty that the results we got are reliable and the simulations where able to accurately capture the reality with enough care.

3.3. Turbulence models

Since the start of this paragraph, we mention the fact that all the following considerations are proposed basing on results present in Figure 6.

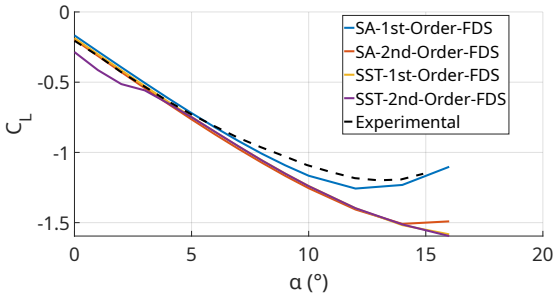

(a) Comparison C_L among different turbulence models.

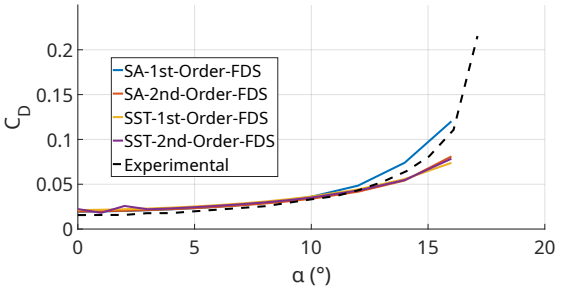

(b) Comparison C_D among different turbulence models.

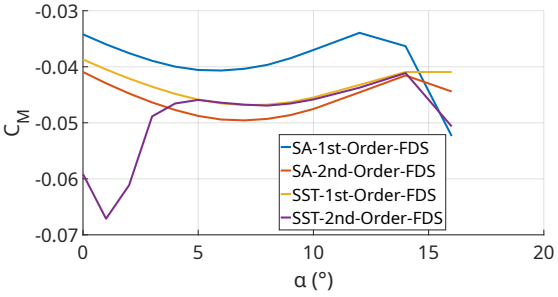

(c) Comparison C_M among different turbulence models.

Figure 6: Comparison of the simulations with different turbulence models.

Regarding turbulence modeling, it is important to emphasize that, for all grids, the dimension of the first cell at the wall (as already mentioned in Section 2.1) was chosen to satisfy the condition $y^+ < 1$. This ensures that wall functions are not required, allowing for a more accurate resolution of the near-wall flow.
One of the key observations from the results is that the **Spalart-Allmaras (SA)** model demonstrates greater accuracy compared to the $\boldsymbol{k-\omega}$ **SST** model in this specific scenario.
The SA model, which is a **one-equation model**, is particularly well-suited for airfoils with attached flows or those exhibiting limited separation, as in this case. On the other hand, the SST model, which is a **two-equation model**, combines a model highly accurate near the wall with another that performs better in the far field. However, for this particular case, the SST model proves less accurate than the SA model.

Observed Issues with the $k-\omega$ SST Model

We mention here two issues observed during our simulations with the $k-\omega$ SST model:

- The **second-order $k-\omega$ SST** model tends to **over-predict** the lift coefficient at low angles of incidence. This occurs because the model is less accurate in conditions dominated by largely attached flow, which is typical for such angles over most of the airfoil surface.
- **SST model struggle to capture the real stall angle**. Specifically, the change in slope of the lift curve during the stall is not accurately captured, making the stall behavior less distinct.

Performance of the Spalart-Allmaras Model

The behavior of the Spalart-Allmaras (SA) turbulence model is particularly noteworthy. Its simplicity and focus on accurately resolving near-wall flows make it well-suited for the aerodynamic characteristics of airfoils, especially under conditions of attached or mildly separated flows. By solving a single transport equation, the SA model minimizes computational cost while delivering reliable predictions for such geometries.
In this case, since the flow separation is confined to a relatively small region, the SA model proves to be both accurate and computationally efficient. In fact, at small angles of attack, the SA model is more accurate than the k-ω SST model which is (as said previously) better suited for predicting large-scale separations, while it struggles at small angles where the flow remains mostly attached.
Additionally, the SA model, being specifically designed for aeronautical applications, exhibits remarkable accuracy in predicting stall. For instance, differently from SST, the SA model successfully predicts it.

3.3.1 Comparison SA first and second order

An interesting feature of the SA model is its performance when using first and second-order discretization schemes. As expected, the second-order discretization provides closer results to the real solution at small angles of attack, where the flow remains attached or only mildly separated.
In particular, the activation of `MUSCLE` reconstruction of $\tilde{\nu}$ improves the accuracy of the solution by considering a linear profile within each computational cell when performing the reconstruction in the REA approach. This process requires the use of a *slope limiter* to handle zones with elevated gradients, such as those generated in the forward region of the flap. In fact, it is important to notice that simulations performed without slope limiters (both for flow variables and turbulence quantities) produced entirely different results, as this problem involves regions with significant gradients. For brevity, we do not include visual representations of the results for these very imprecise simulations, but it was interesting to mention it.
While the second-order scheme excels in such conditions, at high angles of attack, where the flow separation becomes significant and the gradients intensify, the first-order discretization of the SA model yields better results. The smoothing effect of the first-order scheme enhances stability under extreme conditions, effectively mitigating the impact of large gradients that can amplify inaccuracies in other models.
In this section, we aim to visualize and analyze the main differences between the first-order and second-order approaches in the Spalart-Allmaras model, remembering that for the standard flow equations the second order approach is fixed. To clarify, the Spalart-Allmaras model solves a transport equation where the primary unknown is $\tilde{\nu}$, a variable related to the turbulent viscosity ν.
The governing equation for the Spalart-Allmaras model,taken from W.David [2] is given by:

$$\frac{\partial \tilde{\nu}}{\partial t} + u_j \frac{\partial \tilde{\nu}}{\partial x_j} = C_{b1}\tilde{S}\tilde{\nu} + \frac{1}{\sigma}\frac{\partial}{\partial x_j}\left[(\nu+\tilde{\nu})\frac{\partial \tilde{\nu}}{\partial x_j}\right] - C_{w1} f_w \left(\frac{\tilde{\nu}}{d}\right)^2, \tag{1}$$

where $\tilde{\nu}$ is the modified turbulent viscosity, and the source terms $\tilde{S}$, f_w, and d are defined as model-specific quantities.

The strain rate magnitude S in 2D is defined as:

$$S = \sqrt{2\left[\left(\frac{\partial u}{\partial x}\right)^2 + \left(\frac{\partial v}{\partial y}\right)^2 + \frac{1}{2}\left(\frac{\partial u}{\partial y} + \frac{\partial v}{\partial x}\right)^2\right]}, \tag{2}$$

where u and v are the velocity components in the x- and y-directions, respectively. Also, we remind that in this case actually there's no time dependent term.
It is also very important to remind the fact that the variable ν appears in the momentum equation to take into account the turbulent induced diffusivity; this information is relevant for the following considerations about the coupling between the equations involved.
As discussed in Subsection 3.1, one of the most challenging features to capture in a problem of this nature is the steep gradients near the Gurney flap. The solver's ability to accurately resolve these gradients is directly linked to the success of the simulation for several reasons.
For instance, in the Spalart-Allmaras equation, the production term for $\tilde{\nu}$ (and consequently for turbulence) is given by $C_{b1}\tilde{S}\tilde{\nu}$. This term depends on the strain rate, S, which is defined by the formula provided earlier. This highlights the dependency of the turbulence model on the accurate resolution of gradients.
When a first-order scheme is employed, $\tilde{\nu}$ is not resolved correctly, even if the Navier-Stokes equations are solved with second-order accuracy. The error in $\tilde{\nu}$ then propagates back into the momentum equations (in an iterative procedure), effectively degrading the overall solution accuracy. As a result, the full second-order accuracy expected from the Navier-Stokes equations is compromised.
This behavior can be observed in Figure 7, which compares the results for $\tilde{\nu}$ between first-order and second-order schemes. In the second-order case, the gradients are captured more accurately and are not overly smoothed by numerical diffusion in the coupled Navier-Stokes and Spalart-Allmaras equations. This leads to higher turbulence levels (S is greater) and slower dissipation. Conversely, in the first-order case, $\tilde{\nu}$ is significantly lower and diffuses rapidly, resulting in a much lower turbulent diffusivity in the wake region after a short distance.

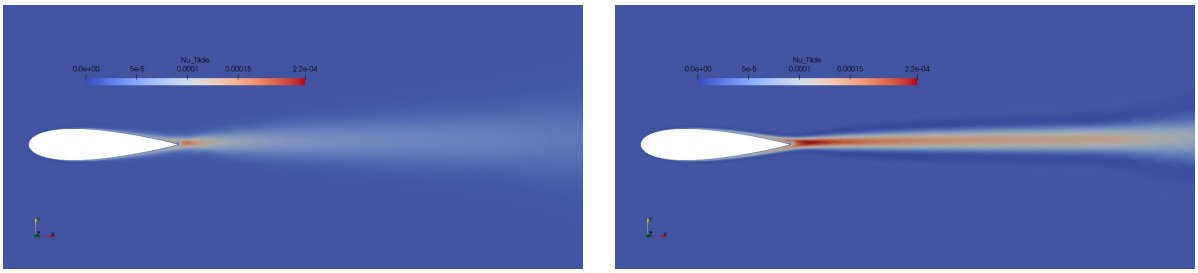

(a) $\tilde{\nu}$ for 1st order simulation.

(b) $\tilde{\nu}$ for 2nd order simulation.

Figure 7: $\tilde{\nu}$ for SA first and second order simulation respectively.

The **coupling** between the Navier-Stokes and Spalart-Allmaras equations affects not only the turbulent variable $\tilde{\nu}$ but also the pressure and velocity fields. This effect is clearly demonstrated in Figure 8, where the second-order simulation exhibits significantly higher pressure gradients compared to the first-order case.

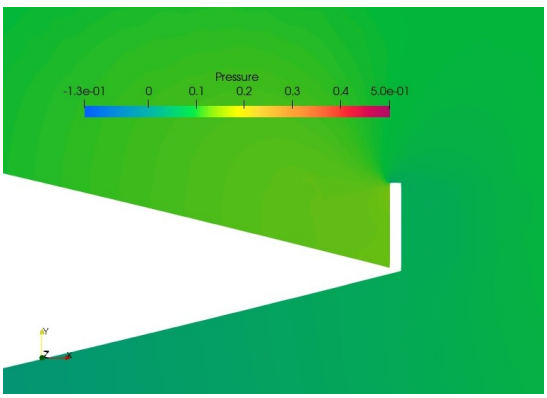

(a) Pressure close to the flap for 1st order simulation.

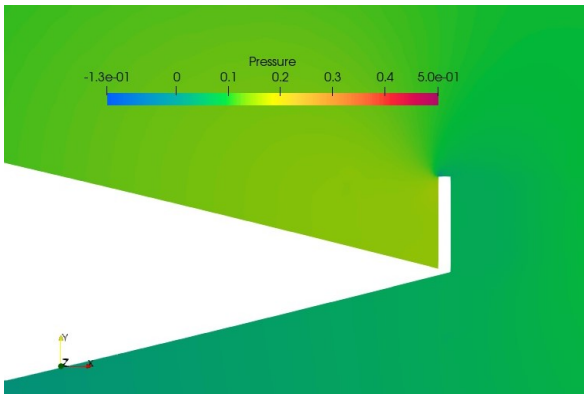

(b) Pressure close to the flap for 2nd order simulation.

Figure 8: Pressure for SA case with first and second order simulation.

3.4. Gurney effect analysis

In this last part concerning the analysis of the results we present the study on the effects of the Gurney flap on an airfoil.
As well known already, the effect of this small flap is to get a significant improvement of vertical force with a small change in drag. This effect can be seen from the plot of the drag and lift coefficients showed before (see Figures 6a, 6b). In fact since the profile is symmetric the result of C_L for a simulation at $\alpha = 0°$ should be zero. This is not true in our case due to the presence of the Gurney and we get a negative overall contribution for the vertical force.

The physical phenomena occurring around the Gurney region can now be analyzed in detail. Specifically, we examine the flow structures near the trailing edge. At low angles of attack the flow generates three vortices: two forms downstream of the flap, while the other develops upstream, leading to the formation of a recirculation bubble.
Conversely, at higher angles, a single, strong counterclockwise vortex is produced downstream of the Gurney, with no distinct counter-rotating vortices observed. This dominant vortex causes the wake region to extend downstream, delaying flow separation. The pressure reduction caused by the vortices enhances suction. Upstream of the flap on the upper surface, a reduction in velocity leads to an increase in pressure, which further contributes to the increase in suction downstream, ultimately boosting downforce. These effects are illustrated in Figure 9, where is possible to see the streamlines along with the τ_{wall}. In particular the regions where $\tau_{wall} \approx 0$ (the blue regions) underline areas where the flow separates. These results have been compared with the ones from S. Mubassira et al. [5], showing good agreement.

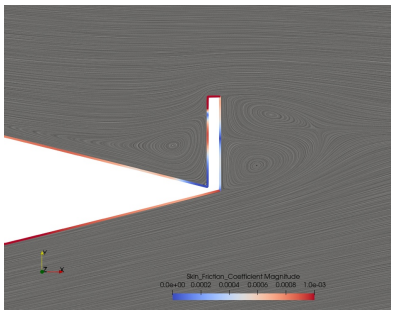

(a) Gurney vortex and τ_{wall} at $\alpha = 0°$.

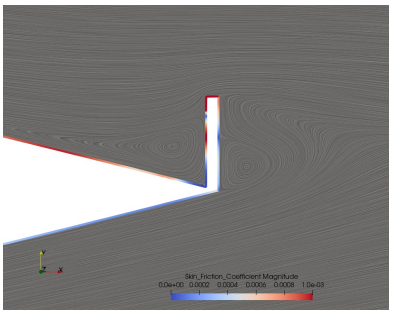

(b) Gurney vortex and τ_{wall} at $\alpha = 4°$.

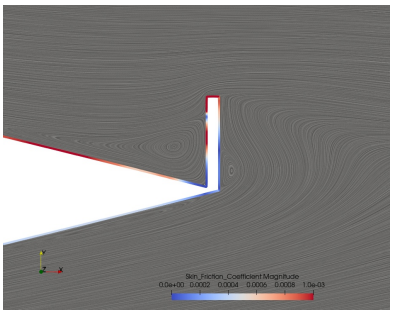

(c) Gurney vortex and τ_{wall} at $\alpha = 8°$.

Figure 9: Comparison of Gurney vortex and τ_{wall} at different angles of attack.

Furthermore for this we can agree with the fact that when $\alpha > 4°$ the effects of separation increase significantly, making our simulation not reliable anymore and the results diverge a little from the experimental ones (as seen in Subsection 3.2). We can further remark this by looking at the $\tilde{\nu}$ coefficient in the region of the Gurney at different angles of attack (Figure 10).

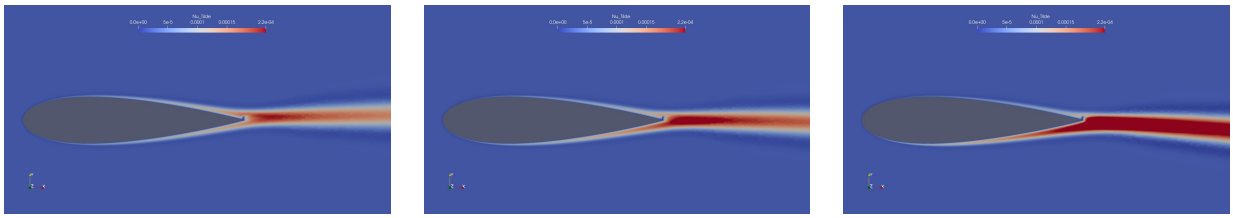

(a) $\tilde{\nu}$ coefficient at $\alpha = 0°$. (b) $\tilde{\nu}$ coefficient at $\alpha = 4°$. (c) $\tilde{\nu}$ coefficient at $\alpha = 8°$.

Figure 10: Comparison of Gurney $\tilde{\nu}$ coefficient at different angles of attack.

4. Further Improvements and Analysis

In this section, we present an initial study outlining potential directions for further developments to deepen the understanding of the effects and roles of Gurney flaps.
Key suggestions for future investigations are as follows:

- **Exploration of alternative Gurney flap geometries**: Investigate the aerodynamic performance of different Gurney flap shapes and sizes to determine their influence on lift, drag, and flow behavior. This could include variations in height, width, and placement relative to the airfoil trailing edge.
  In Section 4.1 we propose one simulation performed by us with the intent to notice the effect of an increase of the flap height on the aerodynamic coefficients.
- **Incorporation of unsteady simulations**: Perform Unsteady Reynolds-Averaged Navier-Stokes (URANS) simulations to capture the unsteadiness of the flow field and highlight its significance. This approach would provide a deeper understanding of transient effects, such as vortex shedding and fluctuating forces, which are crucial in analyzing the dynamic behavior of airfoils with Gurney flaps.
  A brief analysis of an URANS has been provided in Section 4.2.

4.1. Geometric study

To further understand the effects of the Gurney flap, the same simulations are performed with the usual NACA 0021 but a Gurney flap height of 2.5% chord length, keeping the same width as in the previous sections (Figure 11a).
Thanks to the parametric settings of the mesh file, the grid is easily obtained with the same properties and a similar quality as the one described in Section 2.1. It is important to mention that due to time issues it was not possible to perform another grid convergence as the one proposed for the smaller Gurney in Section 2.1. We however rely on the same grid-size used before with the assumption that the small change in geometry do not cause big changes in the simulation behavior. To ensure correctness of the results they have been validated once again with those of J. Balduzzi et al. [1].

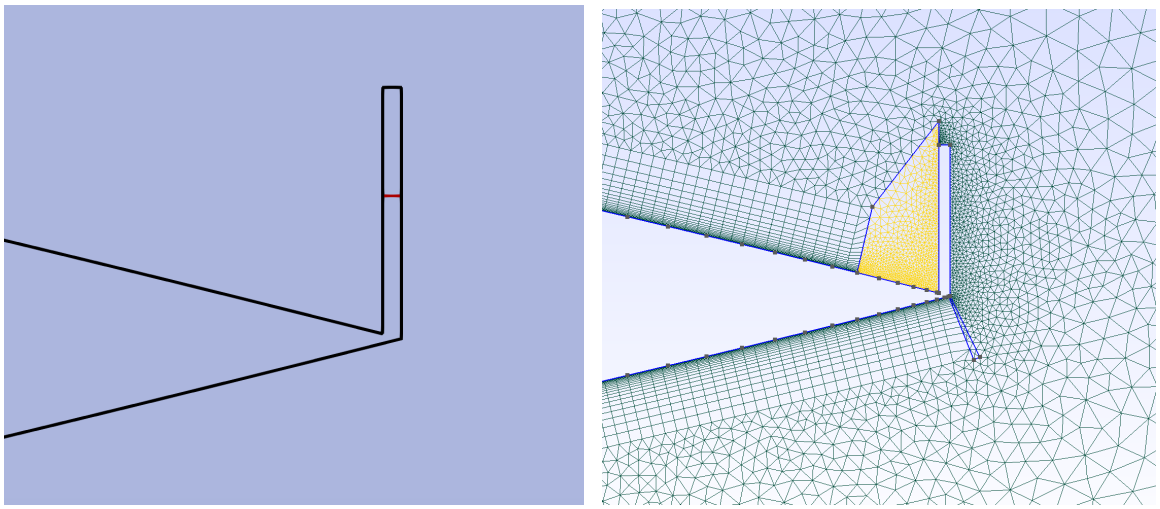

(a) Gurney flap 1.4% (red line) vs 2.5%.

(b) Gurney flap 2.5% grid detail.

Figure 11: Illustration of the new geometry and grid.

Concerning the validation, in Fig.12, we can notice how the drag matches the experimental data accurately (at least far from the stall range), whereas the C_L behavior is not well captured for $\alpha > 4°$, this is likely caused by the presence of a more turbulent flow that is not properly simulated by the steady RANS equations, as already seen in Section 3.2.

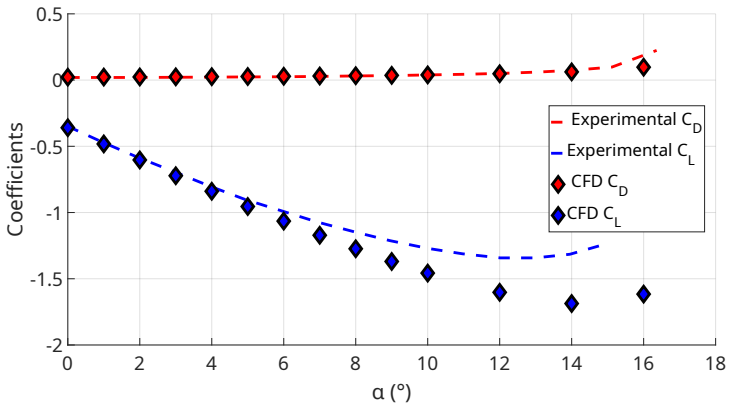

Figure 12: Validation of the Gurney flap at 2.5%c between sperimental and J. Balduzzi et al. [1].

In Figure 13a and 13b we can see how the modulus of the lift coefficient is noticeably increased, almost doubled, to the expenses of a slight increase in the drag coefficient.
To better see this we can refer to Figure 13d where the aerodynamic efficiency is plotted against AOA up to 4°, the angle up to which the results are very accurate for both geometries.
We can clearly observe how, despite the higher aerodynamic resistance, the taller flap produces a much higher lift to drag ratio for every angle of attack, in agreement with the reference results of J.Balduzzi et al. [1].

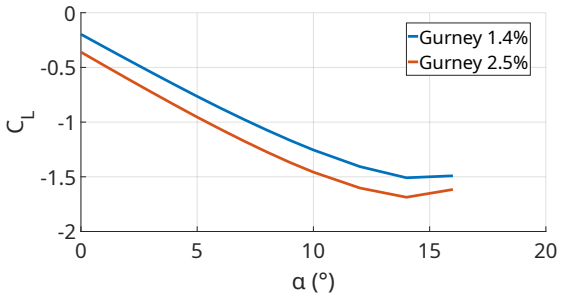

(a) C_L comparison.

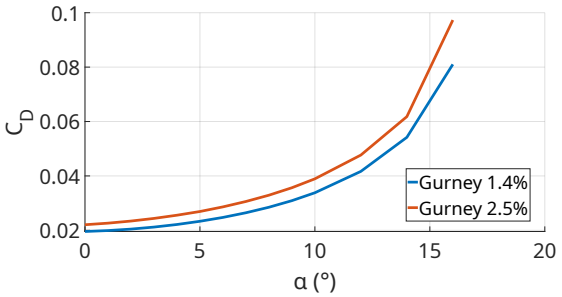

(b) C_D comparison.

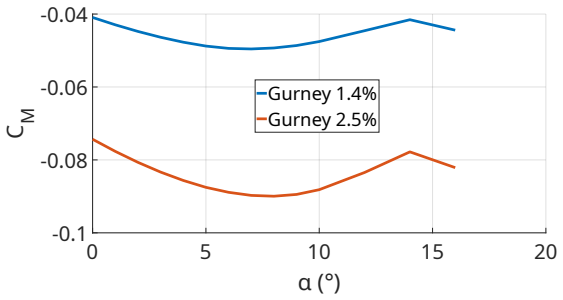

(c) C_M comparison.

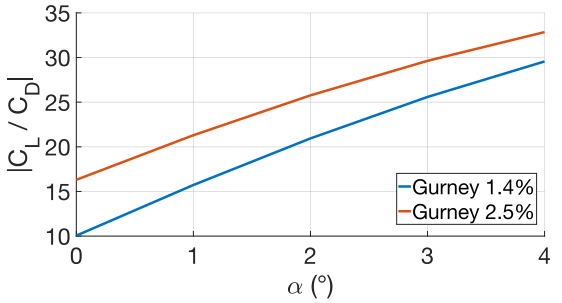

(d) Aerodynamic efficiency comparison.

Figure 13: Aerodynamic coefficients and efficiency comparison between Gurney flap at 1.4%c and 2.5%c.

4.2. Extension to Unsteady RANS (URANS)

To gain deeper insights into the effects of the Gurney flap, it is essential to perform an unsteady RANS (URANS) analysis. It is important to emphasize that the following discussion pertains to an **initial attempt** to conduct such a simulation, and the results presented are neither validated nor confirmed to be accurate. The primary intent is to **qualitatively** illustrate the inherent unsteadiness of the phenomenon, as captured in this preliminary analysis and set the basis for potential further and more accurate studies in the future.

Notably, even at an angle of attack of 0°, flow separation is observed near the Gurney flap. This separation is predominantly driven by the pressure peak generated upstream of the flap.

In Table 1 below, we outline some key aspects of the simulation setup and the specific modifications made to adopt the unsteady approach:

Parameter	**Setting used**
Time step size	$10e-4$
Inner iterations within the time step	80
Time marching scheme	DUAL TIME STEPPING 2ND ORDER

Table 1: Temporal features of the URANS simulation setup.

The flow evolution over time is depicted at selected reference instants in Figure 14, highlighting the transient behavior induced by the Gurney flap. As said before, these visualizations taken from our URANS are primarily qualitative, intended to emphasize that steady-state simulations significantly deviate from capturing the true dynamics of the phenomenon.

One of the main challenges in conducting URANS simulations is the significant computational power required. These simulations demand high CPU performance and considerable RAM capacity, especially when advanced 2nd-order time-stepping schemes are employed to ensure accuracy. The large data volume generated during the simulation further increases memory and processing requirements, making computational efficiency a key consideration.

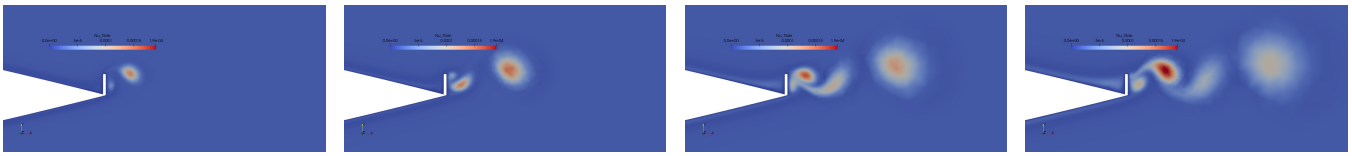

(a) $\tilde{\nu}$ at $t = 3s$. (b) $\tilde{\nu}$ at $t = 6s$. (c) $\tilde{\nu}$ at $t = 9s$. (d) $\tilde{\nu}$ at $t = 12s$.

Figure 14: $\tilde{\nu}$ at different time-steps.

5. Conclusions

To conclude this report we firstly recap the answers to the initial questions proposed in Section 1.
In particular the analysis on the different turbulence models applied to this geometry proved the fact that turbulence plays an important role in the study of external aerodynamics. We indeed experienced that changing the turbulence model led to relevant changes in the results. After all our analysis we can conclude that the best turbulence model for our case is the Spalart Allmaras at second order. This showed an incredibly good coherence with the experimental data provided by J. Balduzzi et al. [1] for both the two geometries considered (Gurney at $1.4\%c$ and $2.5\%c$).
Concerning instead the Gurney effect we proved its relevant effect in gaining aerodynamic efficiency, accessing the physics behavior and the reasons why this happens due to the presence of the vortices before and after the flap.

All this studies gave us the capability to carry out the entire process of a CFD simulation, from the generation of a mesh, the iterative process to reach grid convergence, the numerics setup with its validation process and the critical analysis of the results. In particular,from this last element we understood that the intrinsic unsteady nature of the problem leads to the need of passing trough unsteady solvers in order to access with more accuracy and detail the characteristics of the flow around this geometry.

After all this analysis we can conclude that the results we got are highly accurate and reliable in the limit of small angles (up to 4°) and the simulations performed were able to answer all our initial questions.

References

[1] J. Balduzzi, D. Holst, P. F. Melani, F. Wegner, C. N. Nayeri, G. Ferrara, C. O. Paschereit, and A. Bianchini. Combined numerical and experimental study on the use of gurney flaps for the performance enhancement of naca0021 airfoil in static and dynamic conditions. *Journal of Engineering for Gas Turbines and Power*, pages 5–6, 2021.

[2] Wilcox David. *Turbulence Modeling for CFD*. DCW Industries Inc., 2006.

[3] Thomas D. Economon. Simulation and adjoint-based design for variable density incompressible flows with heat transfer. *AIAA*, pages 5–6, 2018.

[4] R. H. Liebeck. Design of subsonic airfoils for high lift. *AIAA*, pages 547–561, 1978.

[5] M. I. Inam S. Mubassira, F. I. Muna. Numerical investigation of aerodynamic characteristics of naca 4312 airfoil with gurney flap. *Journal of Engineering Advancement*, pages 6–7, 2021.

[6] J.Montefort T. Liu. Thin-airfoil theoretical interpretation for gurney flap lift enhancement. *Journal of Aircraft*, 2007.